where fractionation is larger and where the observed isotopic anomalies are more modest[4]. A major puzzle in the study of noble gases in presolar diamond has always been that, in the case of xenon, overabundances in the light isotopes ('Xe-L') accompany those in the heavy ones ('Xe-H'), but that—in the case of krypton—'Kr-H' is accompanied by what seems a deficit rather than an overabundance of the light isotopes ^{78}Kr and ^{80}Kr relative to s-only ^{82}Kr (refs 4, 27). A first inspection of the changes afforded by taking isotopic fractionation into account[28] indicates that this puzzle may go away and that Kr-L does exist after all, while there may be little (if any) argon associated with anomalous krypton and xenon. □

Methods

The nanodiamonds—obtained from the Scientific Research Institute of Technical Physics (Snezhinks, Russia)—were produced as ultradispersed detonation diamonds[21] (UDD) by detonation synthesis from explosives, with a mean size of ~4 nm. For the implantation an ordinary ion gauge set-up was used, with an axial tungsten cathode surrounded by accelerating grid and cylindrical tantalum collector. Implantation was from a flow of noble gases (estimated ion intensities, He:Ar:Kr:Xe ≈ 150:50:1:1) into a $\sim 3\times10^{-4}$ g cm^{-2} nanodiamond layer deposited from a colloidal suspension onto part of the inner surface of the collector. With an energy of ~700 eV, the range of the ions in diamond is of the order of the grain radius, according to calculations using the TRIM code[29], except for He with a somewhat larger range. After implantation the diamonds were scraped off the collector. Gases were released by vacuum pyrolysis and analysed for the abundance and isotopic composition of noble gases by standard noble-gas mass spectrometry[4,30].

For the implantation, gases were introduced from a reservoir at about one bar pressure into the diffusion-governed regime of the ion source at 5×10^{-4} mbar. Further calibrations will be required in order to decide whether the small isotopic fractionation (relative to atmospheric isotopic composition) observed for the gases in the low-temperature peak (Fig. 2)—which closely follows an $m^{1/2}$ fractionation law, where m is atomic mass—is associated with flow conditions or with the implantation process itself.

Received 5 February; accepted 24 May 2001.

1. Anders, E. & Zinner, E. Interstellar grains in primitive meteorites: diamond, silicon carbide, and graphite. *Meteoritics* **28,** 490–514 (1993).
2. Ott, U. Interstellar grains in meteorites. *Nature* **364,** 25–33 (1993).
3. Zinner, E. in *Astrophysical Implications of the Laboratory Study of Presolar Materials* (eds Bernatowicz, T. J. & Zinner, E.) 3–26 (American Institute of Physics, Woodbury, New York, 1997).
4. Huss, G. R. & Lewis, R. S. Noble gases in presolar diamonds I: Three distinct components and their implications for diamond origins. *Meteoritics* **29,** 791–810 (1994).
5. Lewis, R. S., Tang, M., Wacker, J. G., Anders, E. & Steel, E. Interstellar diamonds in meteorites. *Nature* **326,** 160–162 (1987).
6. Verchovsky, A. B. *et al.* C, N, and noble gas isotopes in grain size separates of presolar diamonds from Efremovka. *Science* **281,** 1165–1168 (1998).
7. Daulton, T. L., Eisenhour, D. D., Bernatowicz, T. J., Lewis, R. S. & Buseck, P. R. Genesis of presolar diamonds: comparative high-resolution transmission electron microscopy study of meteoritic and terrestrial nano-diamonds. *Geochim. Cosmochim. Acta* **60,** 4853–4872 (1996).
8. Tielens, A. G. G. M., Seab, C. G., Hollenbach, D. J. & McKee, C. F. Shock processing of interstellar dust: diamonds in the sky. *Astrophys. J.* **319,** L109–L113 (1987).
9. Nuth, J. A. III & Allen, J. E. Jr Supernovae as sources of interstellar diamonds. *Astrophys. Space Sci.* **196,** 117–123 (1992).
10. Ozima, M. & Mochizuki, K. Origin of nanodiamonds in primitive chondrites: (1) Theory. *Meteoritics* **28,** 416–417 (1993).
11. Matsuda, J. -I., Kusumi, A., Yajima, H. & Syono, Y. Noble gas studies in diamonds synthesized by shock loading in the laboratory and their implications on the origin of diamonds in ureilites. *Geochim. Cosmochim. Acta* **59,** 4939–4949 (1995).
12. Matsuda, J. -I., Fukunaga, K. & Ito, K. Noble gas studies in vapor-growth diamonds: comparison with shock-produced diamonds and the origin of diamonds in ureilites. *Geochim. Cosmochim. Acta* **55,** 2011–2023 (1991).
13. Frick, U., Mack, R. & Chang, S. Noble gas trapping and fractionation during synthesis of carbonaceous matter. *Proc. Lunar. Planet. Sci. Conf.* **X,** 1961–1973 (1979).
14. Bernatowicz, T. J. & Fahey, A. J. Xe isotopic fractionation in a cathodeless glow discharge. *Geochim. Cosmochim. Acta* **50,** 445–452 (1986).
15. Weigel, A. *et al.* Noble gas systematics in planetary atmospheres: Simulation of fractionation mechanisms using ion implantation. *Lunar Planet. Sci.* [CD-ROM] **XXIX,** abstr. 1900 (1998).
16. Bernatowicz, T. J. & Hagee, B. E. Isotopic fractionation of Kr and Xe implanted in solids at very low energies. *Geochim. Cosmochim. Acta* **51,** 1599–1611 (1987).
17. Ponganis, K. V., Graf, T. & Marti, K. Isotopic fractionation in low-energy ion implantation. *J. Geophys. Res.* **102,** 19335–19343 (1997).
18. Futagami, T., Ozima, M., Nagai, S. & Aoki, Y. Experiments on thermal release of implanted noble gases from minerals and their implications for noble gases in lunar soil grains. *Geochim. Cosmochim. Acta* **57,** 3177–3194 (1993).
19. Koscheev, A. P., Gromov, M. D., Herrmann, S. & Ott, U. Trapping and isotope fractionation of noble gases in synthetic analog of presolar diamond grains. *Lunar Planet. Sci.* [CD-ROM] **XXXI,** abstr. 1551 (2000).
20. Verchovsky, A. B., Wright, I. P., Fisenko, A. V., Semjonova, L. F. & Pillinger, C. T. Ion implantation into presolar diamonds: experimental simulation. *J. Conf. Abstr.* [CD-ROM] **5,** abstr. 1050 (2000).
21. Lyamkin, A. I. *et al.* Production of diamonds from explosives. *Sov. Phys. Dokl.* **33,** 705–706 (1988).
22. Koscheev, A. P. & Ott, U. Mechanism of noble gas release during pyrolysis of nanodiamond grains. *Meteorit. Planet. Sci.* **35,** A92 (2000).
23. Clayton, D. D. Origin of heavy xenon in meteoritic diamonds. *Astrophys. J.* **340,** 613–619 (1989).
24. Howard, W. M., Meyer, B. S. & Clayton, D. D. Heavy-element abundances from a neutron burst that produces Xe-H. *Meteoritics* **27,** 404–412 (1992).
25. Ott, U. Interstellar diamond xenon and timescales of supernova ejecta. *Astrophys. J.* **463,** 344–348 (1996).
26. Guillois, O., Ledoux, G. & Reynaud, C. Diamond infrared emission bands in circumstellar media. *Astrophys. J.* **521,** L133–L136 (1999).
27. Frick, U. Anomalous krypton in the Allende meteorite. *Proc. Lunar Sci. Conf.* **VIII,** 273–292 (1977).
28. Huss, G. R., Ott, U. & Koscheev, A. P. Implications of ion-implantation experiments for understanding noble gases in presolar diamonds. *Meteorit. Planet. Sci.* **35,** A79–A80 (2000).
29. Ziegler, J. F., Biersack, J. P. & Littmark, U. *The Stopping Range of Ions in Solids* (Pergamon, Tarrytown, New York, 1985).
30. Schelhaas, N., Ott, U. & Begemann, F. Trapped noble gases in unequilibrated ordinary chondrites. *Geochim. Cosmochim. Acta* **54,** 2869–2882 (1990).

Acknowledgements

We thank S. Herrmann for assisting with the noble-gas measurements, G.R. Huss and A.B. Verchovsky for discussions, and R.S. Lewis and A.P. Meshik for comments on the manuscript. This work was partially supported by the Russian Foundation of Basic Science and by the German DFG.

Correspondence and requests for materials should be addressed to U.O. (e-mail: ott@mpch-mainz.mpg.de).

Two-dimensional imaging of electronic wavefunctions in carbon nanotubes

Serge G. Lemay*, Jorg W. Janssen*, Michiel van den Hout*, Maarten Mooij*, Michael J. Bronikowski†, Peter A. Willis†, Richard E. Smalley†, Leo P. Kouwenhoven* & Cees Dekker*

** Department of Applied Physics and DIMES, Delft University of Technology, Lorentzweg 1, 2628 CJ Delft, The Netherlands*
† Center for Nanoscale Science and Technology, Rice Quantum Institute, Departments of Chemistry and Physics, MS-100, Rice University, PO Box 1892, Houston, Texas 77251, USA

The drive towards the development of molecular electronics is placing increasing demands on the level of control that must be exerted on the electronic structure of materials. Proposed device architectures ultimately rely on tuning the interactions between individual electronic states, which amounts to controlling the detailed spatial structure of the electronic wavefunctions in the constituent molecules[1,2]. Few experimental tools are available to probe this spatial structure directly, and the shapes of molecular wavefunctions are usually only known from theoretical investigations. Here we present scanning tunnelling spectroscopy measurements of the two-dimensional structure of individual wavefunctions in metallic single-walled carbon nanotubes; these measurements reveal spatial patterns that can be directly understood from the electronic structure of a single graphite sheet, and which represent an elegant illustration of Bloch's theorem[3] at the level of individual wavefunctions. We also observe energy-dependent interference patterns in the wavefunctions and exploit these to directly measure the linear electronic dispersion relation of the metallic single-walled carbon nanotube.

We deposited nanotubes from a sonicated dichloroethane suspension[4] onto atomically flat Au(111) surfaces. To reduce disorder in the observed electronic band structure (J.W.J., S.G.L.,

L.P.K. and C.D., unpublished results), we used high-purity carbon nanotubes that had been catalytically grown in high-pressure carbon monoxide[5]. To increase the electronic energy-level spacing, individual metallic single-walled nanotubes (SWNTs) were shortened to less than 40 nm by applying locally a short bias pulse of 6.5 V between the tip of the scanning tunnelling microscope (STM) and the sample[6] (Fig. 1a). Topography (Fig. 1b) and scanning tunnelling spectroscopy (STS) measurements were then performed as a function of position on a two-dimensional grid with sub-ångstrom resolution.

The STS technique measures the tunnelling differential conductance (dI/dV) between the STM tip and the sample as a function of sample bias V, where dI/dV is to a good approximation proportional to the local density of electronic states (LDOS) of the sample[7]. For a system described by discrete electronic wavefunctions $\psi_j(\mathbf{r})$, the measured STS signal is thus given by

$$\frac{dI}{dV}(V,\mathbf{r}) \propto \sum_{|eV-\epsilon_j|<\delta} |\psi_j(\mathbf{r})|^2 \qquad (1)$$

where $\mathbf{r}$ is the position coordinate and δ is the experimental energy resolution. When δ is less than the energy level spacing $\epsilon_{j+1} - \epsilon_j$, the sum in equation (1) reduces to a single term, and a two-dimensional measurement of the LDOS at fixed energy ϵ_j corresponds to a spatial map of $|\psi_j|^2$.

Figure 1c shows a measurement of dI/dV versus V performed on a metallic SWNT. The presence of a series of sharp peaks in the LDOS indicates that the effective energy resolution δ is indeed smaller than the confinement-induced level spacing in our short SWNTs. Figure 1d–f shows three representative images of dI/dV versus position at fixed V. These correspond to spatial maps of different individual molecular wavefunctions $|\psi_j|^2$. All of the measured wavefunction images show a quasi-periodic pattern of spots with similar spacing, but each image also exhibits unique features such as stripes, alternating rows of bright and dim spots, or a rectangular supercell. The discrete wavefunctions of carbon nanotubes thus appear to display a variety of spatial patterns.

The wavefunction images differ from the image of the atomic lattice of the nanotube, shown in Fig. 1b. The nature of this difference is most clearly evident in a reciprocal-space representation. A SWNT can be thought of as a single plane of graphite rolled into a cylinder; the hexagonal lattice of carbon atoms is sketched in Fig. 2A, and the Fourier transform of an STM image of the atomic

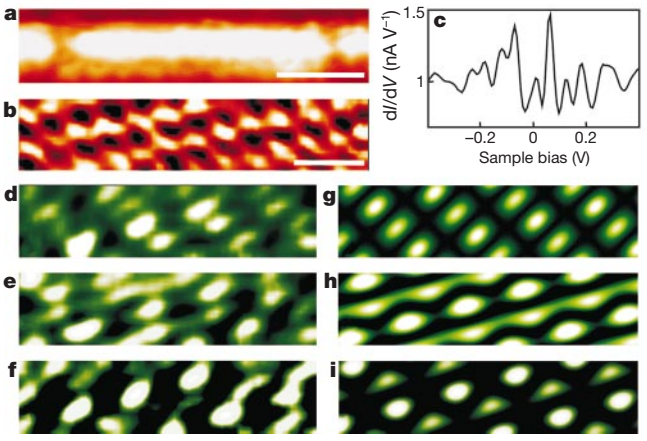

Figure 1 Energy-resolved images of individual molecular wavefunctions. **a**, Constant-current topographic image of a metallic SWNT that has been cut to a length of 34 nm. This nanotube has an apparent height of 1.1 nm and a chiral angle of 12°. The data were recorded in constant-current mode using a feedback current of 200 pA and a sample voltage of –200 mV. Scale bar, 10 nm. **b**, Constant-current topographic image of the atomic lattice of the shortened nanotube. Scale bar, 0.5 nm. **c**, Scanning tunnelling spectroscopy measurement. The vertical axis is approximately proportional to the LDOS; we attribute sharp peaks to discrete 'particle-in-a-box' electronic states. The data are a spatial average over the area shown in **b**. **d**–**f**, Energy-resolved images of the individual states at energies of –96, 30 and 96 meV, respectively, illustrating the variety in the appearance of individual wavefunctions. These dI/dV images are obtained using a lock-in technique. The periodicity of these images differs from that of the simultaneously acquired atomic lattice image shown in **b**. **g**–**i**, Calculated spatial maps of $|\psi_j(\mathbf{r})|^2$ based on equation (2). The characteristic features of each image are well reproduced. The calculation does not include a slow variation of the observed structure with position, described in detail in Fig. 3. All measurements were performed in an Omicron LT-STM operated at 4.6 K using Pt/Ir tips cut in air. Featureless I–V characteristics were observed on the Au(111) substrate—both before and after STS measurements were performed on the SWNT. All data reported in this Letter are from the same sample (except Fig. 2d). Consistent results were obtained on a second shortened SWNT sample. In addition, similar two-dimensional patterns were observed on disordered ropes of SWNTs.

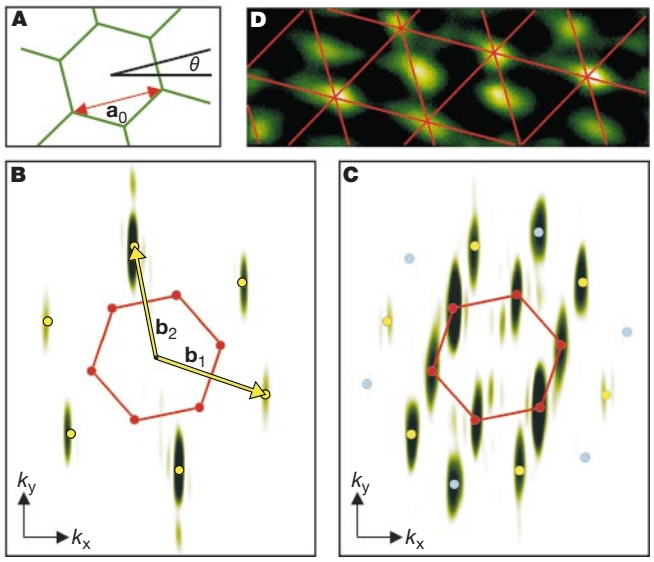

Figure 2 Comparison of the observed spatial structure with theory. The horizontal direction corresponds to the longitudinal axis of the SWNT. **A**, Real-space hexagonal lattice and definitions of the lattice spacing a_0 and of the chiral angle θ. **B**, Two-dimensional Fourier transform of a topographic image of the atomic lattice. Peaks appear at wavevectors corresponding to reciprocal lattice vectors $\mathbf{G} = m\mathbf{b}_1 + n\mathbf{b}_2$, where m, n are integers (filled yellow circles). The red hexagon indicates the border of the first Brillouin zone, and the red dots correspond to the calculated Fermi wavevectors $\pm\mathbf{k}_n^0$. The peaks in the data are elongated in the traverse (k_y) direction because the SWNT is intrinsically narrow in that direction. **C**, Two-dimensional Fourier transform of a wavefunction image at a sample bias $V = 64$ mV. As per equation (2), the wavefunction $\psi_j(\mathbf{r})$ is dominated by six Fourier components with wavevectors corresponding to the corners of the first Brillouin zone (red dots). Additional Fourier components corresponding to the second harmonics of these six fundamental components also appear (yellow and blue dots) because the experiment is sensitive to $|\psi_j(\mathbf{r})|^2$ instead of $\psi_j(\mathbf{r})$. For clarity, the high-intensity peak at $\mathbf{k} = 0$ was removed from the Fourier transforms in **B** and **C**. **D**, Relation between a measured wavefunction image and the calculated Fourier components. Each set of parallel lines represents the wavefronts of one of the 'fundamental' Fourier components $\pm\mathbf{k}_n^0$ represented by red dots in **C**. The spacing and orientation of these wavefronts were determined from a topographic measurement of the atomic lattice; only the phase of each wave was adjusted to coincide with the position of the bright spots in the energy-resolved image. Some spots appear between crossing red lines. These are due to the second harmonics corresponding to the yellow and blue dots in **C**, and are present because we measure $|\psi_j(\mathbf{r})|^2$. Image **D** was obtained on a SWNT rope and is shown here because it is relatively wide in the transverse (y) direction, thus providing a clearer real-space illustration than our measurements on individual SWNTs.

lattice is shown in Fig. 2B. As expected, the Fourier transform exhibits bright spots at wavevectors **k** corresponding to the reciprocal lattice vectors **G**. The Fourier transform of a wavefunction image, shown in Fig. 2C, shows new peaks at smaller wavevectors. In particular, the additional Fourier components in the wavefunction images have wavevectors that coincide with the corners of the first Brillouin zone (represented by a red hexagon in Fig. 2B, C).

Nanotube wavefunction images have been calculated before[8,9], but not yet experimentally verified. One-dimensional STS line scans have been reported for the special case of an 'armchair' nanotube[10], and were interpreted in terms of a simple one-dimensional particle-in-a-box model. We now show that the full two-dimensional structure of measured wavefunctions as reported in our work can be understood, for arbitrary chirality, from a careful examination of the electronic structure of a single plane of graphite.

Band-structure calculations indicate that the Fermi surface of a plane of graphite consists of only six discrete points corresponding to the corners of the hexagonal first Brillouin zone. We label these wavevectors $\pm\,\mathbf{k}_n^0$, where $n = -1, 0, 1$. A wavefunction $\psi_j(\mathbf{r})$ at the Fermi level of a finite-sized SWNT is a superposition of Bloch waves, and can be written in the form[9] $\psi_j(\mathbf{r}) = 2Re[u_{j,n}(\mathbf{r})\exp(i\mathbf{k}_n^0\cdot\mathbf{r})]$. Here $u_{j,n}(\mathbf{r})$ is a function with the periodicity of the atomic lattice. It follows that the Fourier transform of $\psi_j(\mathbf{r})$ contains Fourier components with wavevectors $\pm\,\mathbf{k}_n^0 + \{\mathbf{G}\}$, where $\{\mathbf{G}\}$ is the set of all reciprocal lattice vectors. But not all of these Fourier components contribute to the measured images. Because Fourier components with larger $|\mathbf{k}|$ decay more rapidly with distance from the SWNT surface, STS images are dominated by the Fourier components with the lowest wavevectors[7]. The measured wavefunctions near the Fermi level are therefore predicted to have the form:

$$\psi_j(\mathbf{r}) = \sum_{n=-1}^{1} (\phi_{j,n}e^{i\mathbf{k}_n^0\cdot\mathbf{r}} + \phi_{j,n}^{*}e^{-i\mathbf{k}_n^0\cdot\mathbf{r}}) \qquad (2)$$

Equation (2) successfully describes the wavefunction images we observe, as demonstrated by the coincidence of the experimental peaks with the calculated dots appearing in the Fourier transform (Fig. 2C). Figure 2D further illustrates in real space the relationship between the Fourier components $\exp(i\mathbf{k}_n^0\cdot\mathbf{r})$ and the periodic structures observed in the measured wavefunctions. It displays a wavefunction image on which lines have been superimposed to represent the lines of constant phase of each of these Fourier components. The predicted orientation and wavelength clearly match the rows of peaks observed in the data. Finally, Fig. 1g–i illustrates that the detailed features of the measured wavefunctions can be reproduced by equation (2): selecting appropriate values of $\phi_{j,n}$ yields a variety of spatial patterns that closely matches the experimental results shown in Fig. 1d–f. Slight differences between experimental (Fig. 1d–f) and calculated (Fig. 1g–i) images can be attributed to residual noise as well as to long-wavelength modulations observed in the measurements (discussed below).

We now turn to variations in the measured wavefunctions as a function of energy, from which we can extract information about the electronic dispersion relation of the SWNTs. The detailed spatial pattern of each wavefunction appears to exhibit slow variations with position that are not accounted for by equation (2). In order to clearly display these variations, we plot in Fig. 3b the LDOS at energy $E = -60$ meV as a function of position along the nanotube axis over a larger range of x than shown in Fig. 1. A slow, sinusoidal-like oscillation is found in addition to the rapid Fermi-wavelength oscillations discussed above. The wavelength of this slow oscillation increases markedly with increasing energy, as can be seen from the plot of the LDOS shown in Fig. 3c.

These energy-dependent features allow us to verify some key features of the band structure of carbon nanotubes. The theoretical dispersion relation of a metallic SWNT is sketched in Fig. 3a; two linear one-dimensional bands cross at the charge-neutrality point E_0. These two bands are orthogonal in a SWNT of infinite length, but in our finite-sized tubes they mix because the atomic structure at the tube ends generally has low symmetry (A. A. Maarouf, N. R. Wilson and C. L. Kane, manuscript in preparation). Each individual wavefunction $\psi_j(\mathbf{r})$ is thus a linear combination of two left- and two right-moving Bloch waves with wavevectors $\pm\,(\mathbf{k}_0^0 \pm \delta\mathbf{k}_j)$, where $\delta\mathbf{k}_j$ is related to the energy ϵ_j by:

$$\delta k_j = (E_0 - \epsilon_j)/\hbar v_F \qquad (3)$$

Here v_F is the Fermi velocity. Superposing waves with slightly different wavevectors $\mathbf{k}_0^0 \pm \delta\mathbf{k}_j$ results in a beating pattern—that is, a rapid oscillation with wavevector $\mathbf{k}_0^0$ modulated by an envelope function with wavevector $\delta\mathbf{k}_j$. The rapid oscillation with wavevector $\mathbf{k}_0^0$ is responsible for the primary structure in our wavefunctions (Figs 1 and 2). The additional slow modulation corresponds to the beating pattern envelope. The oscillations observed here are thus the result of quantum-mechanical interference at the level of individual electronic wavefunctions. They are fundamentally different from those reported near step edges of metallic surfaces[11,12], where the interference pattern instead originates from a continuum of states with a fixed phase relation at the step edge.

Measuring δk_j as a function of ϵ_j provides us with the means to directly extract the dispersion relation near the Fermi level for this individual SWNT. The result is shown in Fig. 3d. The dispersion

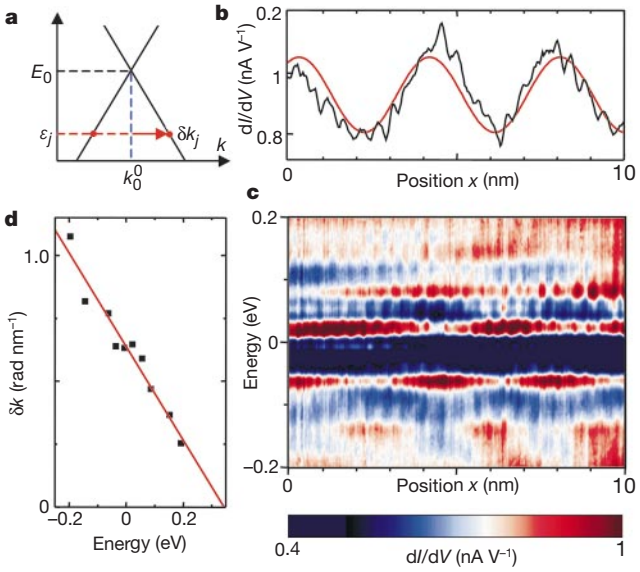

Figure 3 Determination of the dispersion relation from the energy dependence of wavefunction images. **a**, Sketch of the calculated one-dimensional band structure of a chiral metallic SWNT near the Fermi level. Two bands cross at the energy E_0. Under our experimental conditions[4], the Fermi energy E_F lies below E_0. Individual wavefunctions are composed of Bloch waves with wavevectors $\pm\,(\mathbf{k}_0^0 \pm \delta\mathbf{k}_j)$, where $\delta\mathbf{k}_j$ is parallel to the axis of the SWNT and varies linearly with energy ϵ_j. **b**, Measurement of dI/dV versus position x along the longitudinal axis of the SWNT for $E = eV = -60$ meV. A low-wavevector modulation is apparent, which we associate with a beating pattern with wavevector $\delta\mathbf{k}_j$. The red line is a fit to $|\psi(x)|^2 = A\cos(2\delta kx + \varphi)$, where φ is an arbitrary phase and the factor of 2 appears because STS probes $|\psi(x)|^2$ rather than $\psi(x)$. **c**, Colour-scale plot of dI/dV versus electron energy E and position x along the longitudinal axis of the SWNT. Two types of features are observed: (1) an energy-independent modulation with wavevector $2k_{0,x}^0$ that appears as vertical stripes (about 20 periods visible), and (2) a slow modulation whose wavevector varies with energy. For example, about 2.5 periods of this envelope are visible at $E = -0.06$ eV. **d**, Dispersion relation δk_j versus E_j. δk_j was obtained from a fit of each peak in **c**, as illustrated in **b**. The red line is a fit to the linear dispersion relation of equation (3), yielding values of $(8.2 \pm 0.7) \times 10^5$ m s^{-1} for the Fermi velocity v_F and 0.34 ± 0.03 eV for the energy of the charge-neutrality point $E_0 - E_F$.

relation is linear, as predicted by equation (3). This measurement is, to our knowledge, the first direct experimental verification of this important property—on which (among other things) the application of Luttinger-liquid theory to carbon nanotubes is based[13,14].

Fitting the measured dispersion relation to equation (3) yields the value of the Fermi velocity in nanotubes, $v_F = (8.2 \pm 0.7) \times 10^5\,m\,s^{-1}$. In a tight-binding description, v_F is related to the π–π overlap energy γ_0 by $v_F = 3^{1/2}\gamma_0 a_0/2\hbar$, where a_0 is the atomic lattice spacing. Our measurement thus corresponds to a value of $\gamma_0 = 2.6 \pm 0.2$ eV. For comparison, determinations of γ_0 based on the energies of van Hove singularities in STS and Raman spectroscopy measurements yield 2.5–2.9 and 2.6–3.0 eV, respectively[15]. Our determination of γ_0 based on a direct measurement of $E(k)$ performed near the Fermi level is therefore in agreement with those based on higher-energy structures. The fit also yields $E_0 - E_F = 0.34 \pm 0.03$ eV for the energy of the charge-neutrality point ($\delta k = 0$), in agreement with previous estimates[4,16].

Analysis of the variation of the energy-level spacing $\epsilon_{j+1} - \epsilon_j$ and of the energy-dependence of the coefficients $\phi_{j,n}$ of our wavefunctions reveals departures from recent theoretical predictions (A. A. Maarouf, N. R. Wilson and C. L. Kane, manuscript in preparation), suggesting that the electronic boundary conditions at the tube ends are energy-dependent. Interference effects have recently been invoked to explain transport measurements on SWNTs[17], but irregularities were observed that could also not be explained by assuming energy-independent boundary conditions. It is likely that harnessing these quantum-mechanical interference effects for practical devices will ultimately require the control of the atomic structure—and hence the electronic boundary conditions—at the nanotube ends. □

Received 4 June; accepted 13 July 2001.

1. Aviram, A. & Ratner, M. Molecular rectifiers. *Chem. Phys. Lett.* **29,** 277–283 (1974).
2. Joachim, C., Gimzewski, J. K. & Aviram, A. Electronics using hybrid-molecular and mono-molecular devices. *Nature* **408,** 541–548 (2000).
3. Bloch, F. Über die quantenmechanik der elektronen in kristallgittern. *Z. Phys.* **52,** 555–600 (1928).
4. Wildöer, J. W. G., Venema, L. C., Rinzler, A. G., Smalley, R. E. & Dekker, C. Electronic structure of atomically resolved carbon nanotubes. *Nature* **391,** 59–62 (1998).
5. Bronikowski, M. J., Willis, P. A., Colbert, D. T., Smith, K. A. & Smalley, R. E. Gas-phase production of carbon single-walled nanotubes from carbon monoxide via the HiPco process: a parametric study. *J. Vac. Sci. Technol. A* **19,** 1800–1805 (2001).
6. Venema, L. C. *et al.* Length control of individual carbon nanotubes by nanostructuring with a scanning tunneling microscope. *Appl. Phys. Lett.* **71,** 2629–2631 (1997).
7. Tersoff, J. & Hamann, D. R. Theory of the scanning tunneling microscope. *Phys. Rev. B* **31,** 805–813 (1985).
8. Rubio, A., Sánchez-Portal, D., Artocho, E., Ordejón, P. & Soler, J. M. Electronic states in a finite carbon nanotube: a one-dimensional quantum box. *Phys. Rev. Lett.* **82,** 3520–3523 (1999).
9. Kane, C. L. & Mele, E. J. Broken symmetries in scanning tunneling images of carbon nanotubes. *Phys. Rev. B* **59,** R1279–R12762 (1999).
10. Venema, L. C. *et al.* Imaging electron wave functions of quantized energy levels in carbon nanotubes. *Science* **283,** 52–55 (1999).
11. Crommie, M. F., Lutz, C. P. & Eigler, D. M. Imaging standing waves in a two-dimensional electron gas. *Nature* **363,** 524–527 (1993).
12. Hasegawa, Y. & Avouris, Ph. Direct observation of standing wave formation at surface steps using scanning tunneling spectroscopy. *Phys. Rev. Lett.* **71,** 1071–1074 (1993).
13. Egger, R. & Gogolin, A. O. Effective low-energy theory for correlated carbon nanotubes. *Phys. Rev. Lett.* **79,** 5082–5085 (1997).
14. Kane, C., Balents, L. & Fisher, M. P. A. Coulomb interactions and mesoscopic effects in carbon nanotubes. *Phys. Rev. Lett.* **79,** 5086–5089 (1997).
15. Dresselhaus, G. *et al.* in *Science and Application of Nanotubes* (eds Tománek, D. & Enbody, R.) 275–295 (Kluwer Academic/Plenum, New York, 2000).
16. Venema, L. C. *et al.* Spatially resolved scanning tunneling spectroscopy on single-walled carbon nanotubes. *Phys. Rev. B* **62,** 5238–5244 (2000).
17. Liang, W. *et al.* Fabry-Perot interference in a nanotube electron waveguide. *Nature* **411,** 665–669 (2001).

Acknowledgements

We thank C. L. Kane for discussions and for making theoretical results known to us before publication. This work was supported by NASA, the Dutch Foundation for Fundamental Research (FOM) and the European Union IST-FET program SATURN.

Correspondence and requests for materials should be addressed to S.L. (e-mail: lemay@mb.tn.tudelft.nl).

Observation of individual vortices trapped along columnar defects in high-temperature superconductors

A. Tonomura*†, H. Kasai*†, O. Kamimura*†, T. Matsuda*†, K. Harada*†, Y. Nakayama†‡, J. Shimoyama†‡, K. Kishio†‡, T. Hanaguri†§, K. Kitazawa†§, M. Sasase‖ & S. Okayasu‖

* *Advanced Research Laboratory, Hitachi Ltd, Hatoyama, Saitama 350-0395, Japan*
† *CREST, Japan Science and Technology Corporation (JST), Kawaguchi, Saitama 332-0012, Japan*
‡ *Department of Applied Chemistry, University of Tokyo, Tokyo 113-8656, Japan*
§ *Department of Advanced Materials Science, School of Frontier Sciences, University of Tokyo, Tokyo 113-0033, Japan*
‖ *Department of Material Science, Japan Atomic Energy Research Institute, Tokai, Naka-gun, Ibaraki 319-1195, Japan*

Many superconductors do not entirely expel magnetic flux—rather, magnetic flux can penetrate the superconducting state in the form of vortices. Moving vortices create resistance, so they must be 'pinned' to permit dissipationless current flow. This is a particularly important issue for the high-transition-temperature superconductors, in which the vortices move very easily[1]. Irradiation of superconducting samples by heavy ions produces columnar defects, which are considered[2] to be the optimal pinning traps when the orientation of the column coincides with that of the vortex line. Although columnar defect pinning has been investigated using macroscopic techniques[3,4], it has hitherto been impossible to resolve individual vortices intersecting with individual defects. Here we achieve the resolution required to image vortex lines and columnar defects in $Bi_2Sr_2CaCu_2O_{8+\delta}$ (Bi-2212) thin films, using a 1-MV field-emission electron microscope[5]. For our thin films, we find that the vortex lines at higher temperatures are trapped and oriented along tilted columnar defects, irrespective of the orientation of the applied magnetic field. At lower temperatures, however, vortex penetration always takes place perpendicular to the film plane, suggesting that intrinsic 'background' pinning in the material now dominates.

There are several methods of directly observing vortices, but none of them can determine the behaviour of individual vortex lines inside superconductors. This is because these methods detect vortices at the superconductor surfaces, even though an attempt has been made to obtain evidence of wandering vortex lines near material defects by using a two-sided Bitter decoration technique to detect the vortex positions on both sides of the film[6]. At present, the only methods which enable the observation of individual vortices and defects inside superconducting thin films are Lorentz microscopy[7] and interference microscopy[8], where the vortex magnetic fields are detected using a penetrating electron beam. However, owing to the low penetration power of the existing 300-kV field-emission electron beam, only a film thinner than the diameter of the vortex magnetic flux (that is, twice the magnetic penetration depth) has been observed. Vortex lines oriented in different directions cannot be distinguished in such a thin film, because the vortex magnetic fields inside it do not change very much.

To obtain clear images of vortices inside thicker films, we have developed a large electron microscope[5]. This 40-ton microscope has a 1-MV field-emission electron beam that has more than twice the penetration power of a 300-kV beam and also the highest brightness ($2 \times 10^{10}\,A\,cm^{-2}\,sr^{-1}$) ever attained. These features of the electron beam have allowed us not only to observe vortices in Bi-2212 films 400 nm thick with high contrast, but also to